Astron. Astrophys. 337, 897–910 (1998)

ASTRONOMY AND ASTROPHYSICS

Magnetic flux tubes evolving in sunspots

A model for the penumbral fine structure and the Evershed flow

R. Schlichenmaier[1⋆], **K. Jahn**[2], **and H.U. Schmidt**[3]

[1] Max-Planck-Institut für extraterrestrische Physik, D-85748 Garching, Germany
[2] Warsaw University Observatory, Al. Ujazdowskie 4, PL-00 478 Warsaw, Poland (crj@astrouw.edu.pl)
[3] Max-Planck-Institut für Astrophysik, Karl-Schwarzschild-Str. 1, D-85748 Garching, Germany

Received 29 January 1998 / Accepted 26 June 1998

Abstract. Assuming that the interchange convection of magnetic flux elements is the physical cause for the existence of filamentary penumbrae in sunspots, we investigate the behavior of an individual fibril embedded in the deep penumbra. The fibril is approximated by a thin magnetic flux tube which evolves dynamically in the environment given by the global magnetostatic model of a sunspot.

Our simulation shows that the flux tube, initially positioned at the penumbra–quiet Sun boundary in the model, will rise through its deep penumbra developing a flow along the tube that points upward beneath the photosphere, and radially outward above the photosphere. Our results suggest that a bright filament may be formed by an extended tail of a penumbral grain. Such filaments are optically thick, hotter than the surroundings, and elevated above a darker background. An upflow in penumbral grains bends horizontally outwards above the photosphere and gradually cools down due to radiative losses leading to a tail that gradually darkens. The plasma flow inside the flux tube then becomes transparent and the tube constitutes a thin elevated flow channel, that can reproduce the observed features of the Evershed effect. We present also a new acceleration mechanism for the Evershed flow. It is demonstrated that a local surplus of gas pressure develops inside the tube as it rises through the specific (superadiabatic and magnetized) penumbral background. The resulting gradient of the gas pressure can drive the flow along the tube.

Key words: sunspots – Sun: magnetic fields – MHD

1. Introduction

A sunspot penumbra seen in high resolution images reveals a small scale fine structure (for a review, see Muller 1992). At a resolution better than $0.5''$, penumbral grains and radially elongated bright and dark filaments become visible. There is some observational evidence that bright filaments consist of a few penumbral grains which are radially aligned (Muller 1973b; Soltau 1982). Penumbral grains exhibit proper motions and migrate inwards, i.e. toward the umbra, with apparent velocities of 300–500 m s^{-1} (Muller 1973a). Muller describes penumbral grains as comet-like structures, having a bright coma and a somewhat dimmer tail, which is always directed radially outwards, i.e. away from sunspot center (see also Fig. 2 in Tritschler et al. (1997)). He states that penumbral grains have a diameter of $0.35''$. However, this value is close to the spatial resolution limit that was achieved in his observations. Grossmann–Doerth & Schmidt (1981) find on the basis of a statistical analysis of penumbral fine structure, that bright and dark filaments have to be smaller than $0.55''$. Using the 1.5 m MacMath telescope, Stachnik et al. (1983) find spatial scales of $0.11''$ within the penumbra. These results rely on power spectra which were obtained using speckle interferometry. Thus, since the spatial dimensions of bright and dark filaments are uncertain, it is impossible to assign reliable values for corrected photospheric intensities and effective temperatures of the penumbral fine structure.

A still not fully understood penumbral phenomenon was discovered by Evershed (1909): photospheric absorption lines show a shift of the line core that turns out to be related to a line asymmetry when dark penumbral structures are observed (Beckers & Schröter 1969; Wiehr & Degenhardt 1994). In recent years evidence has accumulated that the Evershed effect must be due to a magnetized plasma flow (Solanki et al. 1994) occurring in thin elevated horizontal channels containing outward flows (Rimmele 1995). The observed asymmetry of the intensity profile can then be explained as the superposition of an unresolved Doppler shifted component and an unshifted main component. Here it is assumed that an individual flow channel cannot be spatially resolved as suggested by many observers (Bumba 1960; Holmes 1963; Schröter 1965; Stellmacher & Wiehr 1980; Wiehr 1995; Balthasar et al. 1997).

The siphon flow mechanism has been proposed to explain the Evershed effect by Meyer & Schmidt (1968). It was studied numerically for stationary flux tubes, which arch from the inner penumbra to the outer penumbral boundary, by numerous authors (e.g., Thomas 1988; Degenhardt 1991; Thomas &

Send offprint requests to: R. Schlichenmaier, Freiburg
⋆ Present address: Kiepenheuer-Institut für Sonnenphysik, Schöneckstr. 6, D-79104 Freiburg, Germany (schliche@kis.uni-freiburg.de)

Montesinos 1993). Hitherto, the stationary siphon flow model is the most broadly accepted explanation for the Evershed effect. For these models it is essential to assume strong magnetic flux concentrations of opposite polarity near the outer edge of the penumbra that can create a gas pressure gradient along the arched flux tube in order to accelerate the plasma. Here, we want to present for the first time a dynamical model in which the plasma is accelerated locally in the penumbra. In our model, the gas pressure gradient that accelerates the flow is naturally caused by the evolution of the flux tube.

The subphotospheric structure of sunspot penumbrae cannot be observed directly. It is deduced by means of numerical models for the overall structure of a spot (see the review of Jahn 1992); models with characteristics at the surface which are concurrent with observations yield some information about the spot's properties in deeper layers (e.g., Jahn 1989; Jahn & Schmidt 1994). Both models and observations of the magnetic field strength and its inclination within the penumbra (e.g., Beckers & Schröter 1969; Schmidt et al. 1992; Title et al. 1993; Lites et al. 1993) indicate that the penumbra cannot be a surface phenomenon. Instead, it has to be deep (Schmidt 1987, 1991).

The averaged photospheric heat flux of the penumbra, $F_{\rm pu} \approx 0.75 F_\odot$, is significantly higher than the corresponding umbral heat flux, $F_{\rm u} \approx 0.23 F_\odot$. Jahn & Schmidt (1994, hereafter JS) proposed a concept of interchange convection of magnetic flux tubes to account for the surplus brightness of the penumbra. Inspired by observations of bright and dark filaments they conjectured that the magnetic field within the penumbra consists of an ensemble of magnetic flux tubes. They surmised that inclined magnetic flux tubes evolve dynamically within the penumbra and are able to transport heat more efficiently than magnetoconvection in the umbra which contains an almost vertical magnetic field. The onset of interchange convection should depend on the slope of the magnetic field lines: Imagine a perturbation acting on a bundle of magnetic field lines being in magnetohydrostatic equilibrium. Since the component of the buoyancy forces acting perpendicular to the tube increases as the flux tube becomes more horizontal, there may exist an angle for which buoyancy forces perpendicular to the tube resulting from a perturbation overcome restoring magnetic forces. Then interchange convection of magnetic flux tubes sets in (see also Rucklidge et al. 1995).

JS constructed the tripartite model for a sunspot which describes self-consistently the three stratifications corresponding to the umbra, the penumbra, and the quiet sun. These three stratifications are in mechanical equilibrium, such that different gas pressures between the adjacent stratifications are balanced by the magnetic pressure. The corresponding magnetic fields are generated by two current sheets, namely the magnetopause, which separates the quiet sun and the penumbra, and the peripatopause, which separates the penumbra and the umbra. Fig. 1 shows a schematic drawing of these current sheets.

All the stratifications are in hydrostatic equilibrium and the heat transport (with varying efficiency) is described by means of the mixing length theory. It is assumed that the peripatopause thermally insulates the umbra, whereas heat exchange along

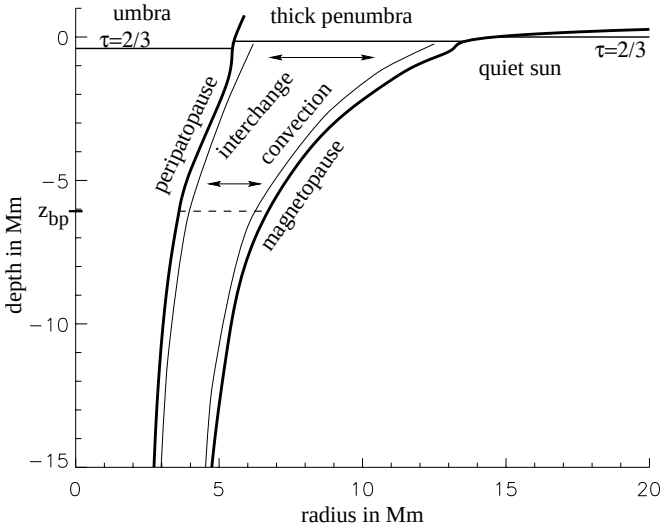

Fig. 1. Sunspot model in a meridional cut. Above $z_{\rm bp}$, the magnetopause transmits heat which is distributed horizontally by the interchange of magnetic flux tubes. Both the peripatopause and the lower part of the magnetopause do not transmit energy (see also Fig. 2 in JS).

the magnetopause is allowed in subphotospheric layers as long as the slope of the magnetopause relative to the vertical exceeds a critical angle of typically 30°, which corresponds to the bottom of the penumbra, $z_{\rm bp}$ (see Fig. 1). Since the energy transport is more efficient in the quiet sun stratification than in the penumbra, the latter is heated. The rate of heating depends on the transmissivity of the magnetopause, which is a free parameter of the model. It is assumed that the transmitted heat is distributed instantaneously on horizontal planes in the penumbra model. Consequently, as it is adopted for the umbra and the quiet sun, also the penumbral thermal stratification varies only with depth. Thus, the surplus brightness of the penumbra in the model is due to a finite transmissivity of the magnetopause. The tripartite model of JS has been successful in reproducing the observed magnetic flux of the spot, the observed radial variation of the mean magnetic field strength, the observed radii of sunspots, and the Wilson depressions of umbra and penumbra. Moreover, interchange convection naturally causes an inhomogeneous penumbra with features that are concurrent with many high resolution observations (e.g., Schmidt et al. 1992; Title et al. 1993; Lites et al. 1993).

The present investigation was started in order to test quantitatively the concept of interchange convection. Numerical investigation of the dynamics of the whole ensemble of magnetic flux tubes is not possible at present. As the natural first step, the discussion presented here is devoted to the evolution of a single magnetic flux tube, which is embedded in a tripartite sunspot. Moreover, we assume the flux tube to be *thin*. The equations that govern the dynamics of a thin magnetic flux tube are described in the next section. We also describe there briefly the numerical realization of the model. Sect. 3 describes the model set-up, i.e. the initial conditions and the boundary conditions, and the resulting evolution of a thin magnetic flux tube. In Sect. 4, we

compare the results of numerical simulations with the observed photospheric features of penumbrae, and argue that our model can reproduce the penumbral fine structure and the Evershed effect. Also, the concept of interchange convection is discussed on the basis of these new results. In the last section we summarize the results emphasizing the observational signatures that are suggested by our model.

2. The model

We start by writing down the full 3-dimensional system of equations for ideal magnetohydrodynamics (MHD) (see, e.g., Priest 1982). In ideal MHD, the electrical conductivity is assumed to be infinite, leading to frozen-in-magnetic fields. Using the substantial (convective) derivative,

$$\frac{\mathrm{d}}{\mathrm{d}t} = \frac{\partial}{\partial t} + \boldsymbol{v}\cdot\nabla \ , \tag{1}$$

and cgs-units, the equations for continuity, induction, equation of motion, entropy equation, divergence free magnetic field, and the equation of state read:

$$\frac{\mathrm{d}\rho}{\mathrm{d}t} = -\rho\nabla\cdot\mathbf{v} \ , \tag{2}$$

$$\frac{\partial}{\partial t}\mathbf{B} = \nabla\times(\mathbf{v}\times\mathbf{B}), \ , \tag{3}$$

$$\nabla\cdot\mathbf{B} = 0 \ , \tag{4}$$

$$\rho\frac{\mathrm{d}\mathbf{v}}{\mathrm{d}t} = -\nabla p + \mathbf{g}\rho + \frac{1}{4\pi}(\nabla\times\mathbf{B})\times\mathbf{B}, \ , \tag{5}$$

$$\rho T\frac{\mathrm{d}S}{\mathrm{d}t} = \rho T\left(\frac{\mathrm{d}S}{\mathrm{d}t}\right)_{\mathrm{rad}} \ , \tag{6}$$

$$p = \frac{\mathcal{R}}{\mu}\rho T + \frac{4\sigma}{3c}T^4 \ . \tag{7}$$

Here, ρ, T, p, $\boldsymbol{B}$, $\boldsymbol{v}$, and $\boldsymbol{g}$ have their usual meaning. S denotes entropy per unit mass, $\mathcal{R}$ the gas constant, $\mu = \mu(\rho, T)$ the mean molecular weight. The second term on the right hand side (RHS) in Eq. (7) describes the radiation pressure, with σ being the Stefan–Boltzmann–constant, and c the speed of light. By taking advantage of the *thin flux tube approximation* (Defouw 1976; Spruit 1981a, 1981b; Ferriz Mas & Schüssler 1989) this 3-dimensional problem can be reduced to a 1-dimensional problem. Doing so, we closely follow the approach of Moreno Insertis (1986, hereafter MI). Furthermore, adopting the tripartite model of JS as a background, we can describe the dynamics of a thin flux tube evolving in a 2-dimensional plane (x,z).

2.1. Walén equation and equation of motion

In a thin magnetic flux tube physical variables vary only along the tube. Thus, the tube constitutes a curve in a plane, and it is appropriate to use a Lagrange representation. As the independent variable, we have chosen the integrated mass, a, along the tube.

The position of a mass element is specified by the vector: $\boldsymbol{x}(a,t) = (x(a,t), z(a,t))$. Then the velocity and tangent vectors are defined as follows:

$$\boldsymbol{v}(a,t) = \left.\frac{\partial\boldsymbol{x}(a,t)}{\partial t}\right|_a \ , \tag{8}$$

$$\boldsymbol{l}(a,t) = \left.\frac{\partial\boldsymbol{x}(a,t)}{\partial a}\right|_t \ . \tag{9}$$

Note, that $\partial/\partial t(...)|_a$ is identical with the substantial derivative, $\mathrm{d}/\mathrm{d}t$, of Eq. (1). The arc length, $\mathrm{d}s$, of a mass element, $\mathrm{d}a$, is given by $\mathrm{d}s = l\cdot\mathrm{d}a$, with $l = |\boldsymbol{l}|$.

Within the thin flux tube approximation, the magnetic field vector in the tube is always parallel to the tube,

$$\boldsymbol{B} = B\hat{\boldsymbol{t}} \ , \tag{10}$$

with the tangent unit vector, $\hat{\boldsymbol{t}} = \boldsymbol{l}/l$. The magnetic flux, ϕ, is conserved along the tube, i.e.,

$$\phi = BA = \mathrm{constant} \ , \tag{11}$$

with A being the cross section of the tube. With the help of Eqs. (9), (10), and (11) one immediately gets,

$$\frac{\boldsymbol{B}}{\rho} = \phi\boldsymbol{l} \ . \tag{12}$$

Finally, one assumes that the total pressure equilibrium of the tube with its surroundings is achieved instantaneously:

$$p + \frac{B^2}{8\pi} = p_{\mathrm{b}} + \frac{B_{\mathrm{b}}^2}{8\pi} \ . \tag{13}$$

The index b denotes background variables.

The continuity and the induction equations combined together yield the Walén equation which can be written with a use of relations given by Eqs. (9) and (12) in the following form:

$$\frac{\mathrm{d}\mathbf{l}}{\mathrm{d}t} = (\boldsymbol{l}\cdot\nabla)\boldsymbol{v} = \frac{\partial\mathbf{v}}{\partial a} \ . \tag{14}$$

The third term of the equation of motion (5) can be simplified using the vector identities:

$$(\nabla\times\mathbf{B})\times\mathbf{B} = B^2\kappa\hat{\mathbf{n}} + \frac{1}{2}\hat{\mathbf{t}}\frac{\partial}{\partial s}B^2 - \frac{1}{2}\nabla B^2 \ , \tag{15}$$

where $\hat{\boldsymbol{n}}$ denotes the normal unit vector as depicted in Fig. 2, and the curvature κ is defined as

$$\kappa\hat{\mathbf{n}} = \frac{\partial\hat{\mathbf{t}}}{\partial s} \ . \tag{16}$$

Then, using the condition of the instantaneous pressure equilibrium (Eq. 13), the equation of motion can be rewritten:

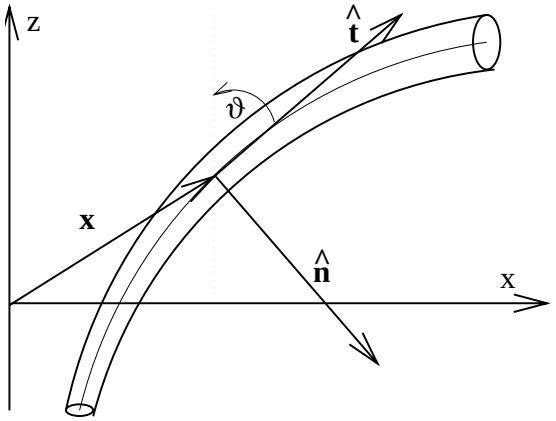

Fig. 2. Geometric variables. The motion of a curved tube within a 2-dimensional plane can be characterized by the position vector $\mathbf{x}(a,t)$. The independent variable a denotes the integrated mass along the tube. $\hat{\mathbf{t}}$ denotes the tangent unit vector, $\hat{\mathbf{n}}$ the normal unit vector, and ϑ the angle between the tangent vector and the vertical.

$$\frac{\mathrm{d}\mathbf{v}}{\mathrm{d}t} = \mathbf{g}\left(1-\frac{\rho_\mathrm{b}}{\rho}\right) + \frac{B^2\kappa}{4\pi\rho}\hat{\mathbf{n}} + \frac{\hat{\mathbf{t}}}{8\pi\rho}\frac{\partial B^2}{\partial s} - \frac{1}{8\pi\rho}\nabla B_\mathrm{b}^2 + \frac{F_D}{\rho}\hat{\mathbf{n}} \tag{17}$$

The additional term on the RHS, F_D/ρ, takes into account the fluid flow around the tube. F_D denotes the drag force. We follow the work of MI (see also Caligari et al. 1995) and use

$$AF_\mathrm{D} = -\rho_\mathrm{b}\frac{d}{2}v_\perp|v_\perp| \ , \tag{18}$$

with d denoting the diameter of the tube.

It is appropriate to decompose the equation of motion into a component parallel to the tube, and a component perpendicular to the tube. For the parallel component, only the first two terms of Eq. (5) are relevant. Hence,

$$\hat{\mathbf{t}}\cdot\frac{\mathrm{d}\mathbf{v}}{\mathrm{d}t} = \left(\frac{\mathrm{d}\mathbf{v}}{\mathrm{d}t}\right)_\parallel = -\frac{1}{\rho l}\frac{\partial p}{\partial a} - g\cos\vartheta \ , \tag{19}$$

where ϑ denotes the angle between the vertical and the tangent vector, $\hat{\mathbf{t}}$ (see Fig. 2). The perpendicular component is obtained by multiplying the final form of Eq. (17) with the normal unit vector $\hat{\mathbf{n}}$:

$$\hat{\mathbf{n}}\cdot\frac{\mathrm{d}\mathbf{v}}{\mathrm{d}t} = \left(\frac{\mathrm{d}\mathbf{v}}{\mathrm{d}t}\right)_\perp = g\sin\vartheta\left(1-\frac{\rho_\mathrm{b}}{\rho}\right) + \frac{B^2}{4\pi\rho}\kappa - \frac{\hat{\mathbf{n}}}{8\pi\rho}\cdot\nabla B_\mathrm{b}^2 + \frac{F_\mathrm{D}}{\rho} \ . \tag{20}$$

Eqs. (14), (19), and (20) determine the time evolution of the tangent vector $\boldsymbol{l}(a,t) = (l_x(a,t), l_z(a,t))$ and the velocity $\boldsymbol{v}(a,t) = (v_x(a,t), v_z(a,t))$. Here, v_x and v_z are obtained by projecting the velocity component according to $\vartheta = \arctan l_x/l_z$. These equations are identical to those derived by MI, except that our tube is embedded in a magnetic background. Therefore, our perpendicular component of the equation of motion contains an additional force (3rd term on RHS of Eq. (20)), which results from the fact, that the gradient of the magnetic pressure in the background exerts a force on the tube. In the magneto-hydrostatic background itself this force is canceled by the magnetic curvature (2nd term on RHS of Eq. (20)). Another subtle difference lies in Eq. (13): in our case, the external pressure is given by the sum of the background gas pressure and the magnetic pressure of the background.

2.2. Entropy equation

The thermodynamic state of a mass element is characterized by $p(a,t)$, $\rho(a,t)$, $T(a,t)$, and $B(a,t)$. These variables are determined by three algebraic equations and one differential equation, i.e. Eqs. (7), (12), (13), and (6).

The thermodynamic parameters of the flux tube are calculated in exactly the same way as the thermodynamics in the background (see Jahn 1989 for details) including the effects of partial ionization on $\gamma = c_p/c_V$ and on the mean molecular weight, $\mu = \mu(\rho,T)$ (note that γ and μ are not assumed to be constant). The chemical composition is assumed according to Stix (1989): $X = 0.7331$, $Z = 0.01669$.

Using the first law of thermodynamics we can write the entropy change in the following form:

$$\frac{1}{c_V}\frac{\mathrm{d}S}{\mathrm{d}t} = \frac{\mathrm{d}\ln T}{\mathrm{d}t} - (\gamma-1)\cdot\frac{\chi_\rho}{\chi_T}\cdot\frac{\mathrm{d}\ln\rho}{\mathrm{d}t} \ . \tag{21}$$

$$\text{with} \qquad \chi_T := \left.\frac{\partial\ln p}{\partial\ln T}\right|_\rho \ , \tag{22}$$

$$\text{and} \qquad \chi_\rho := \left.\frac{\partial\ln p}{\partial\ln\rho}\right|_T \ . \tag{23}$$

This expression is substituted into the entropy equation (6). After eliminating the total derivatives $\mathrm{d}\ln p/\mathrm{d}t$ and $\mathrm{d}\ln T/\mathrm{d}t$, that result from differentiating Eqs. (7), (12), and (13), one finally obtains

$$\left(-\frac{2}{\beta}-\gamma\chi_\rho\right)\frac{\mathrm{d}\ln\rho}{\mathrm{d}t} = \frac{\chi_T}{c_V}\left(\frac{\mathrm{d}S}{\mathrm{d}t}\right)_\mathrm{rad} - \frac{1}{p}\frac{\mathrm{d}P_\mathrm{b}}{\mathrm{d}t} + \frac{2}{\beta}\frac{\mathrm{d}\ln l}{\mathrm{d}t} \ . \tag{24}$$

Note that the background is hydrostatic, $\partial P_\mathrm{b}/\partial t = 0$, so that $\mathrm{d}P_\mathrm{b}/\mathrm{d}t = (\mathbf{v}\cdot\nabla)P_\mathrm{b}$, i.e., the temporal change of P_b is only due to the motion of a Lagrange point in the 2D plane.

2.2.1. Heat exchange by radiation

Since radiation is the dominant physical process in the solar photosphere, radiative heat exchange of the tube with the surroundings has to be taken into account. We do this by adopting

the relaxation time approach by Spiegel (1957, also used by Degenhardt 1991 and Thomas & Montesinos (1993)). For a homogeneous atmosphere in local thermodynamic equilibrium, the inverse damping factor of a temperature perturbation can be identified with a radiative relaxation time,

$$t_{\rm rad} = \frac{c_p}{16\tilde{\kappa}\sigma T^3}\,\left[1-\tau\cdot\mathrm{arccot}(\tau)\right]^{(-1)}\quad , \tag{25}$$

where $\tilde{\kappa}$ is the Rosseland mean opacity (Huebner et al. 1977). For small differences between the two temperatures, the entropy change by radiation is then given by,

$$\left(\frac{\mathrm{d}S}{\mathrm{d}t}\right)_{\rm rad} = \frac{c_p}{t_{\rm rad}T}(T_{\rm b}-T)\quad . \tag{26}$$

2.3. Numerical treatment

The evolution of a thin magnetic flux tube is given by 5 differential equations (two components of Eqs. (14), (19), (20), and (24)) and 3 algebraic equations ((7), (12), and (13)), which are solved for the 8 unknown variables $\boldsymbol{l}(a,t)$, $\boldsymbol{v}(a,t)$, $p(a,t)$, $\rho(a,t)$, $T(a,t)$, and $B(a,t)$. The tube's curvature, κ, is given by

$$\kappa = \frac{1}{l^3}\cdot\left(l_z\frac{\partial l_x}{\partial a} - l_x\frac{\partial l_z}{\partial a}\right)\quad . \tag{27}$$

It is appropriate to use a staggered grid (see MI), in which $\boldsymbol{x}$ and $\boldsymbol{v}$ are discretized on the boundaries of a cell, and the thermodynamical state, i.e. p, T, ρ, B, and $\mathbf{l}$ in the center of the cells. The time integration is done explicitly in two steps. First, the quantity f is calculated for an intermediate step, $f^{n+1/2} = f^n + (\frac{\mathrm{d}f}{\mathrm{d}t})^n\cdot\mathrm{d}t/2$. Then, the full time step is calculated, $f^{n+1} = f^n + (\frac{\mathrm{d}f}{\mathrm{d}t})^{n+1/2}\cdot\mathrm{d}t$. The time step used adapts itself, securing that the Courant-Friedrichs-Lewy-criterion for stability is satisfied for each cell, $dt \le \min(\mathrm{d}s/v_s, \mathrm{d}s/v_{\rm A})$. Here, $\mathrm{d}s$ denotes the arclength of one cell, $v_s = \sqrt{\chi_\rho c_p/c_V}\cdot\sqrt{p/\rho}$ the sound velocity, and $v_{\rm A} = B/\sqrt{4\pi\rho}$ the Alfvén velocity. Simultaneously, the time step is forced to be smaller than the radiation relaxation time, $t_{\rm rad}$. Once, $\boldsymbol{l}^{n+1}$, $\boldsymbol{v}^{n+1}$, and ρ^{n+1} are known, B^{n+1} is determined by Eq. (12) and the position vector, $\boldsymbol{x}^{n+1}$, that fixes the background variables, is obtained by integrating the velocity in time. With B^{n+1}, $p_{\rm b}^{n+1}$, and $B_{\rm b}^{n+1}$, Eq. (13) yields the gas pressure, p^{n+1}. The Saha equations determine the ionization fractions of hydrogen and helium, and thereby the mean molecular weight μ and the specific heat ratio γ. The proper pair of μ^{n+1} and T^{n+1} is found by iterating the equation of state, given by Eq. (7). The Saha equations and the iteration scheme are described in more detail in Schlichenmaier (1997).

2.4. Embedding the tube in a tripartite model

To follow the evolution of the flux tube in the penumbra we embed it in a tripartite sunspot model. Here, the idea is that we take a bundle of magnetic field lines from the sunspot model. These field lines are initially in magneto-hydrostatic equilibrium and form a physical entity, being described by a thin magnetic flux tube in ideal MHD. The parameters of the particular tripartite model we used are listed in Table 1, for an illustration see Fig. 1 in JS.

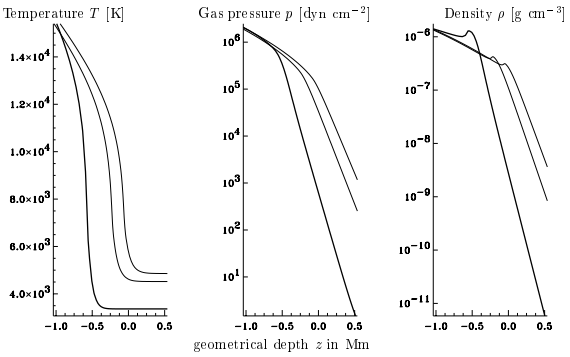

Fig. 3. Thermodynamic variables of the background. A sunspot is approximated by three different stratifications, i.e., the umbra (thick line), the penumbra (regular line), and the quiet sun (thin line).

Table 1. Parameters of background model (cf. JS)

Parameter	Symbol	Value
total magnetic flux	$\Phi_{\rm tot}$	$1\cdot10^{22}$ Mx
magnetic flux of penumbra	$\Phi_{\rm pu}$	$0.75\,\Phi_{\rm tot}$
Wilson depression of umbra †	$W_{\rm u}$	-470 km
Wilson depression of penumbra	$W_{\rm pu}$	-150 km
radius of penumbra at $z=W_{\rm pu}$	$R_{\rm pu}$	13 500 km
radius of umbra at $z=W_{\rm u}$	$R_{\rm u}$	5000 km
transmissivity	ϵ	0.7
lower boundary of model	$z_{\rm bot}$	$-20\,000$ km
upper boundary of model	$z_{\rm top}$	800 km
bottom of penumbra	$z_{\rm bp}$	$-6\,000$ km
B at the bottom of model	$B_{\rm bot}$	15 kG
B at the center in photosphere	$B_{\rm cen}$	2700 G

† $z=0$ km corresponds to the photosphere ($\tau=2/3$) in the quiet sun and decreases inwards.

The thermodynamic stratifications for the umbra, the penumbra, and the quiet sun are prescribed by the tripartite model. Within these stratifications the pressure, $p_{\rm b}(z)$, the density, $\rho_{\rm b}(z)$, and the temperature, $T_{\rm b}(z)$ depend only on depth. Level $z=0$ km corresponds to $\tau=2/3$ level of the quiet sun and decreases downwards. Fig. 3 shows the dependences of $T_{\rm b}$, $p_{\rm b}$ and $\rho_{\rm b}$ on z for the different stratifications in the vicinity of the photosphere. The thermodynamic variables inside the tube, at the center of each cell, are obtained with a use of logarithmic splines defined on the background discretization. The tube lying along the magnetopause is illuminated by the quiet sun on one side. This effect is taken into account in the radiative heat exchange.

The background magnetic field strength, $B_{\rm b}(x,z)$, depends on the radial distance, x, and on depth, z. The radial distance x is defined to be zero at the center of the sunspot model. $B_{\rm b}(x,z)$ for a certain position is determined using a bilinear interpola-

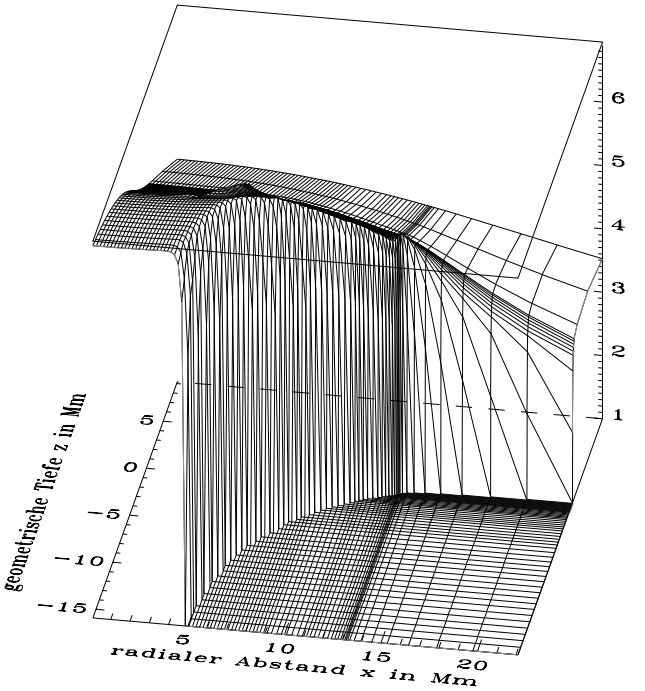

Fig. 4. The background magnetic pressure. $B_{\rm b}^2/8\pi$, is shown as a logarithmic surface plot versus the radial distance, x, and depth, z. For the quiet sun, we set $\log(0) = 1$.

tion. The magnetic pressure, $B_{\rm b}^2/8\pi$, of the used background model is shown in Fig. 4 as a surface plot. One can clearly see the jump across the magnetopause from finite field strength in the penumbra to a vanishing field in the quiet sun. The current sheets, i.e. the magnetopause and the peripatopause, constitute discontinuities for the magnetic pressure, $B_{\rm b}^2/8\pi$, the gas pressure, $p_{\rm b}$, the temperature, $T_{\rm b}$, and the density, $\rho_{\rm b}$. But note, that when crossing the current sheets horizontally, the total pressure (gas plus magnetic) is constant.

3. The evolution of a thin magnetic flux tube embedded in a sunspot

An ensemble of magnetic flux tubes is assumed to participate in interchange convection. As a first step we restrict the study to simulations of the evolution of a single flux tube. In this contribution, we present the results obtained for one specific flux tube and concentrate mainly on its photospheric behavior.

3.1. Initial configuration

The results presented in this section have been obtained for the tube with a magnetic flux $\phi = 2 \cdot 10^{16}$ Mx. That corresponds to a diameter of $d = 2 \cdot \sqrt{\phi/B\pi} = 50$ km, for a magnetic field strength equal to 1000 G. Initially, the tube lies along the magnetopause. Hydrostatic equilibrium along the tube is satisfied since the distribution of the density and temperature is identical with the penumbral stratification:

$$\begin{aligned} t=0:\ \rho(x,z) &= \rho_{\rm b,penumbra}(z) \\ T(x,z) &= T_{\rm b,penumbra}(z) \\ p(x,z) &= p_{\rm b,penumbra}(z) \end{aligned}$$

Magnetostatic equilibrium, i.e., the cancellation of the second and third term on the RHS of Eq. (20), is an intrinsic property of the tripartite model, and can be realized numerically with an accuracy which is sufficient, but limited by the interpolation procedures. The magnetic field strength is given by the total pressure equilibrium across the magnetopause,

$$t=0:\ B(x,z) = \sqrt{8\pi}\sqrt{p_{\rm b,quiet\ sun}(z) - p_{\rm b,penumbra}(z)}\ .$$

The model-tube extends down to a depth of $z = -15$ Mm at a radial distance of $x = 4.8$ Mm. The upper end is placed at a radial distance of $x = 24$ Mm and at a height of $z = 0.3$ Mm above the photosphere ($\tau = 2/3$) of the quiet sun. The intersection of the tube with the photosphere coincides initially with the outer edge of the penumbra model.

3.1.1. Boundary conditions

The lower end of the tube, which is placed at the local position of the magnetopause at $z = -15$ Mm deep in the convection zone, is held fixed, i.e. the mass element at the lower boundary has zero velocity for all times. At the upper boundary, we apply a free boundary condition: The time derivative of the tangent vector, $\mathrm{d}\mathbf{l}/\mathrm{d}t$, is extrapolated and the total force at the last grid point equals the total force at the last but one grid point. In case of an outflow, mass elements reaching $x = 27$ Mm are cut off. That implies that the number of grid elements gradually decreases, if an outflow is present.

3.1.2. Numerical tests

The results presented in this section were obtained using 1033 grid points, being distributed equidistantly in mass for $z > z_{\rm switch} = -1$ Mm and equidistantly in arclength below that depth. It has been tested that the evolution is the same for finer grids and does not depend on the particular choice of the depth, $z_{\rm switch}$ (Schlichenmaier 1997).

When the radiative heat exchange is switched off, entropy becomes a constant of motion. Since the entropy of the system is given by its thermodynamic properties, the conservation of entropy per discretized cell can be checked independently from the code (Schlichenmaier 1997). For this run, the code preserves entropy to a relative accuracy of less than 10^{-4}.

3.2. Time series

Fig. 5a–c shows the time series of our simulation. Each image shows the shape of the tube. The diameter of the tube has been magnified by a factor of 12, for better visibility. The gray-coding

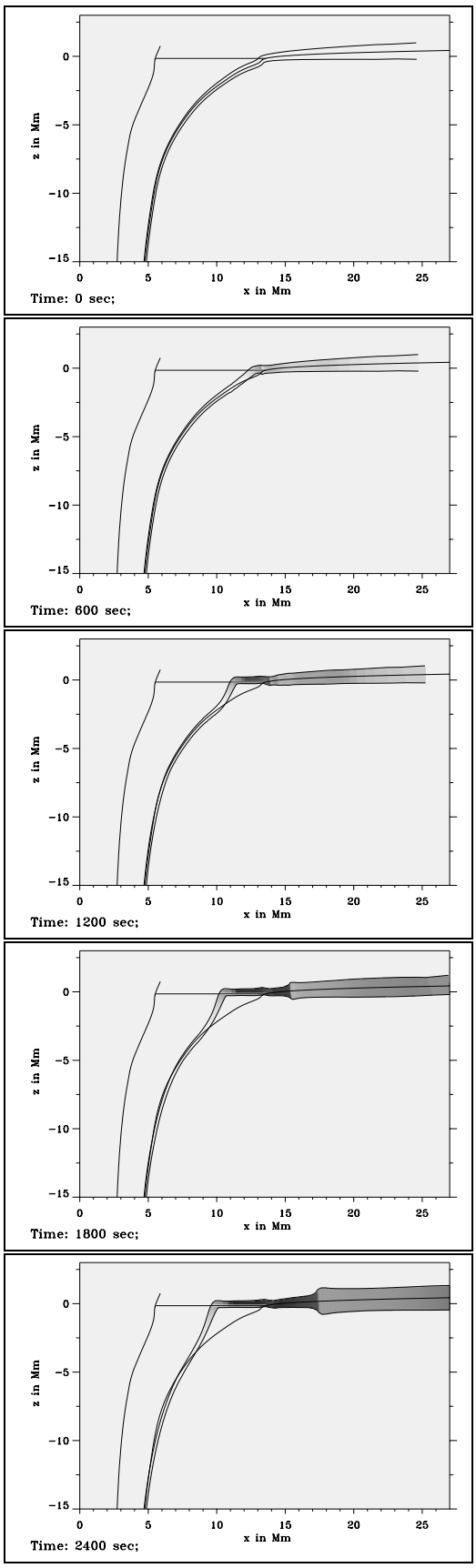
z in Mm
x in Mm
Time: 0 sec;
Time: 600 sec;
Time: 1200 sec;
Time: 1800 sec;
Time: 2400 sec;

5a)

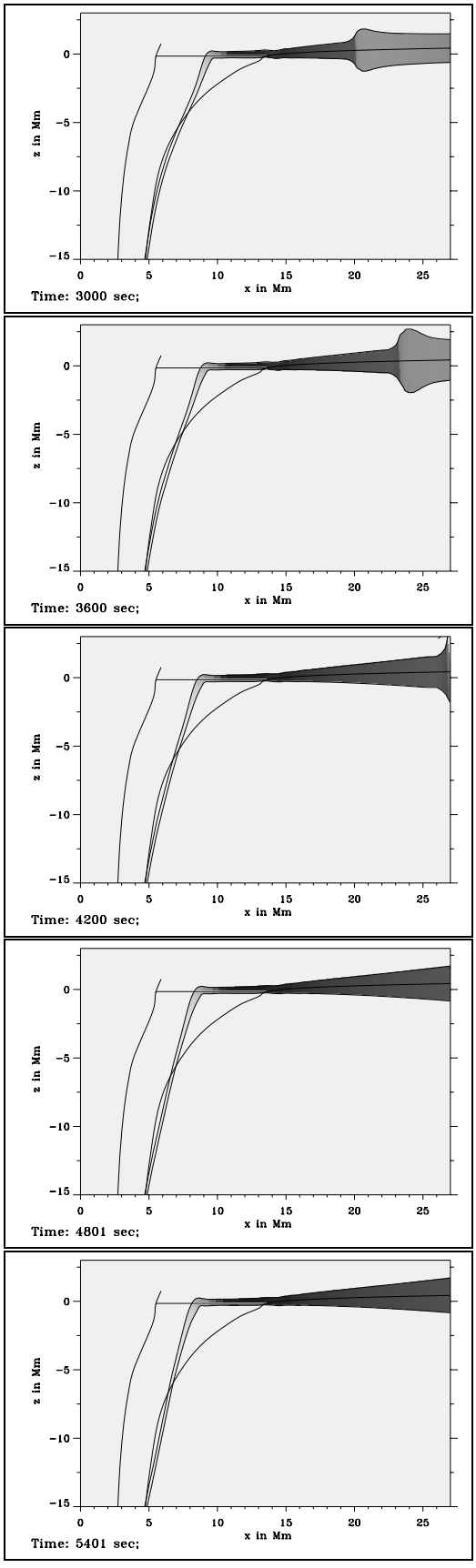
z in Mm
x in Mm
Time: 3000 sec;
Time: 3600 sec;
Time: 4200 sec;
Time: 4801 sec;
Time: 5401 sec;

5b)

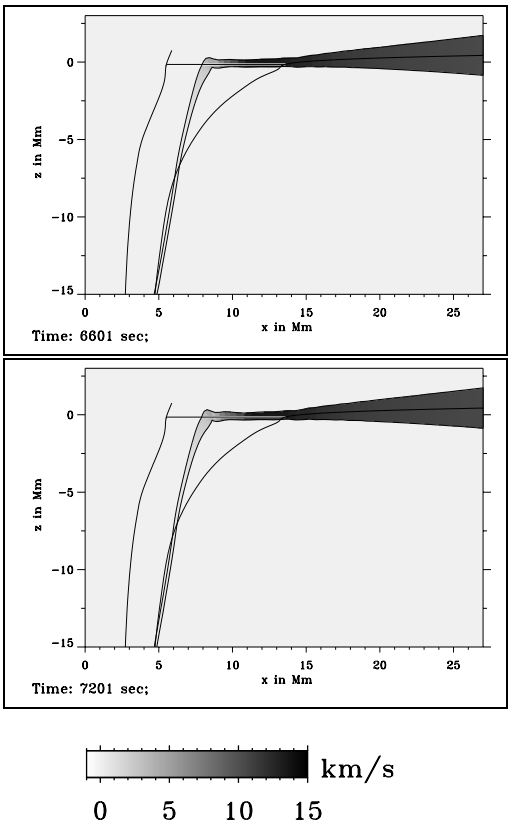

5c)

Fig. 5a–c. Time series of the evolution of a flux tube that contains $\phi = 2 \cdot 10^{16}$ Mx, and initially lies along the magnetopause. Starting just below the photosphere the tube rises, thereby causing the footpoint of the tube to migrate radially towards the umbra. While it rises, a flow along the tube develops, being indicated by the gray-coding of the tube. The background-gray corresponds to 0 km s^{-1}. The flow is directed upwards and outwards. At the outer edge of the penumbra the flow velocity becomes as high as 14 km s^{-1}.

represents the velocity field along the tube. The background-shading represents zero velocity, while darker coding corresponds to positive velocities which point upwards and outwards. Images are plotted every 600 s.

3.2.1. The onset of evolution caused by radiation

Even though initially the tube is in magnetohydrostatic equilibrium, it will start to rise because of the radiative exchange of heat. Part of the tube is illuminated by the underlying hotter quiet sun so that it heats up and expands relatively fast. That leads to a decrease of density inside the tube as compared to the outside, and the buoyancy (first term on RHS of Eq. (20)) causes the tube to rise. The region where the ascending motion appears first is determined by an interplay between the radiative relaxation time, $t_{\rm rad}$, the temperature difference, $T(z) - T_{\rm b}(z)$, and the superadiabaticity, $\delta = \nabla - \nabla_{\rm ad}$. Since radiation is most effective near the photosphere, the radiative relaxation time (see Eq. (25)) is the shortest there. Superadiabaticity, being the cause of convective instability, is largest in the surface layers – within the first few hundred kilometers below the photosphere. The temperature difference between the quiet sun and the umbra, being a measure for the rate of heating, is largest near the photospheric level of the penumbra, i.e., at $z = -150$ km. Therefore, the tube gains buoyancy at the fastest rate just below the photosphere and there the tube will start to rise first. That can be seen in the second image of Fig. 5a.

3.2.2. Initial stages of the evolution

Below the photosphere, the stratification is convectively unstable (superadiabatic) and the tube's rise accelerates. Above the photosphere, the stratification is convectively stable, and moreover, the tube's density increases due to radiative losses. Therefore, the tube's rise decelerates rapidly in the atmosphere. Approximately 100 km above the photosphere, a new equilibrium is found for the tube, in which the downward-acting buoyancy force is neutralized by the upward-acting gradient of the background magnetic pressure (third term of RHS in Eq. (20)). Simultaneously, the footpoint of the tube (i.e. the intersection of the tube with the photosphere at $\tau = 2/3$), moves radially inwards toward the umbra.

3.2.3. Build-up of surplus gas pressure inside the rising tube

A positive flow velocity along the tube develops as the tube rises. It reaches a maximum of 14 km s^{-1} at the outer edge of the penumbra at later stages of the evolution. The onset of this longitudinal flow results from an enhanced gas pressure gradient along the tube, which builds up locally at the place where the tube rises into the photosphere. In order to understand this phenomenon, one has to realize that the tube finds itself (locally) in a strongly superadiabatic environment characterized by a very small gas pressure scale height (of the order of 100 km) which is much smaller than the scale height of the magnetic pressure (approximately 3 000 km). Note also, that below the photosphere the gas pressure dominates the magnetic pressure, i.e. $\beta > 1$.

The tube stays in total (gas + magnetic) pressure equilibrium as it rises (cf. Eq. (13)) and it must expand, because of the decreasing pressure in the background. Since the decrease of the total background pressure is dominated by the gas pressure, the magnetic pressure, $B^2/8\pi$, inside the tube gets smaller than the background magnetic pressure, $B_{\rm b}^2/8\pi$. In consequence, the gas pressure inside, p, must build up relative to the background gas pressure, $p_{\rm b}$. Note, that the background gas pressure is constant horizontally within the penumbra.

Since the part of the tube lying above the photosphere does not rise, it becomes almost horizontal between the footpoint, at $x_{\rm fp}$, and the outer edge of the penumbra, at $x_{\rm oe}$, i.e. $p_{\rm b}(x_{\rm fp}) \simeq p_{\rm b}(x_{\rm oe})$. Near the outer edge of the penumbra the gas pressure inside the tube does not change, $p(x_{\rm oe}) = p_{\rm b}(x_{\rm oe})$, whereas the gas pressure is greatly enhanced in the vicinity of the footpoint, $p(x_{\rm fp}) > p_{\rm b}(x_{\rm fp})$, since there the tube has risen through the strongly superadiabatic region. The resulting gas

pressure gradient accelerates a horizontal outflow along the tube which is accompanied by an upflow in subphotospheric layers. This upflow is maintained by the superadiabatic background stratification. The gas pressure gradient in the horizontal part of the tube is sustained by radiative losses which decrease the internal energy (and the gas pressure) of the matter flowing along the tube.

3.2.4. Centrifugal force and magnetic tension

The migration of the footpoint is governed by three forces acting perpendicular to the tube (the gradient of the background magnetic field can be neglected here). First, at the turning point, i.e. slightly above the footpoint, where the tube bends horizontally, magnetic curvature force is positive (cf. Fig. 2) and it decelerates the migration of the footpoint. Second, the longitudinal flow exerts a centrifugal force at the turning point. The centrifugal force term stems from the advection term in Eq. (1), $\boldsymbol{v}\cdot\nabla$:

$$\boldsymbol{v}\cdot\nabla\boldsymbol{v} = \frac{\hat{\boldsymbol{t}}}{2}\frac{\partial v^2}{\partial s} + v^2\kappa\hat{\boldsymbol{n}} \quad .$$

The first term gives the inertia force along the tube, and the second term is the centrifugal force, which is the inertia force perpendicular to the tube.

Third, the buoyancy being a vertical force that acts perpendicular to the tube dominates the rise as long as the tube is highly inclined with respect to the vertical. As the time series shows, the inward migration of the footpoint ceases at $t = 3\,600$ s. Here, the buoyancy becomes negligible, because of the almost vertical orientation of the subphotospheric part of the tube. Thus, in later stages of the evolution, the perpendicular component of the equation of motion near the turning point is governed only by the centrifugal and the magnetic curvature forces. It is interesting to note, that the centrifugal force neutralizes the magnetic curvature force when the flow velocity equals the Alfvén velocity.

3.2.5. Formation of a shock front above the photosphere

The time series shows a shock front that develops beyond the outer edge of the penumbra. It forms at $x = 15$ Mm after 1 800 s and migrates outwards with a velocity of roughly 3 km s^{-1}. While it migrates outwards and upwards, the shock front accelerates and reaches $\approx$6 km s^{-1} at the outer (upper) boundary. Based on simple physical arguments, the mere existence of this shock wave can be explained as follows. Assume you have a stationary flow upwards along the tube. Due to continuity, the flow velocity, $v_\parallel$, would then increase according to $v_\parallel \sim 1/\rho$, whereas the Alfvén velocity v_A scales as $v_\mathrm{A} \sim B/\sqrt{\rho}$. Now, ρ decreases exponentially and, not so important, B decreases linearly with height. Thus, $v_\parallel$ being smaller than v_A at some initial height, increases more rapidly than v_A. At some point, $v_\parallel$ has to become superalfvénic. In a magnetic flux tube the critical flow velocity along the tube is given by the tube speed, $v_\mathrm{t} = v_\mathrm{A}\cdot v_\mathrm{s}/\sqrt{v_\mathrm{A}+v_\mathrm{s}}$ (e.g., Ferriz Mas 1988), implying that a superalfvénic flow is supercritical at the same time. Having a supercritical flow that collides with plasma which is at rest initially has to result in a shock front. As this shock-front accelerates the plasma, it migrates outwards and leaves the computational domain after 4 200 s.

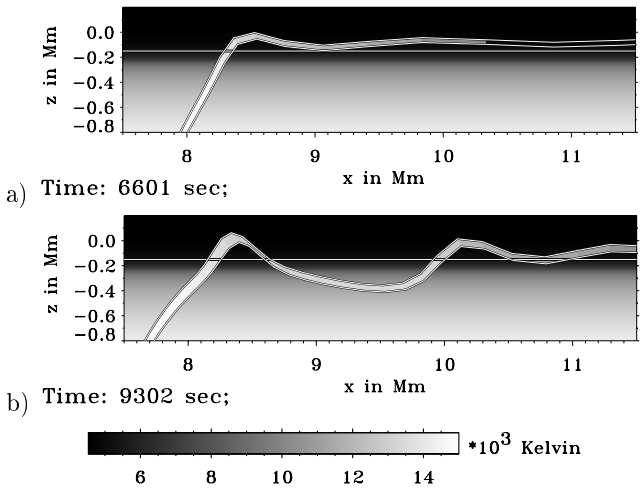

Fig. 6a and b. Two snapshots of the flux tube and the temperature profile. As the Alfvén velocity increases at the footpoint due to the continuous upflow along the tube, the centrifugal force at the turning point ($x \approx 8.4$ Mm) exceeds the magnetic tension, leading to overshooting. **a** shows the phase in which the overshoot is convectively stable at $t = 7\,500$ s, while **b** visualizes the instable phase at $t = 9\,300$ s, where the tube dives back into the subphotospheric stratification. The gray coding refers to temperature according to the shading bar.

In the present contribution we do not make any attempt to realistically describe shock waves. But it is clear that the shock does not influence the dynamics happening near the penumbral photosphere for several reasons. First, the shock front is a *consequence* of the acceleration of plasma within the penumbra, rather than the cause of the longitudinal flow. Second, the density decreases exponentially with height, and therefore the inertia within the photospheric penumbra is much to large to be affected by the dynamics happening hundreds of kilometers above the photosphere. And after all, the flow velocity upstream of the shock is supercritical, i.e., the penumbral photosphere doesn't know about the shock front.

The flow is decelerated within the shock and the gas pressure increases there. That leads to a local expansion of the tube at the shock front. Such an expansion should be counteracted by magnetic tension forces inside the tube. However, within the thin flux tube approximation such forces are neglected and nothing prevents the tube from infinite expansion at the shock front. Therefore, we have included the magnetic tension forces inside the tube fictitiously by changing the background pressure, P_b: At the location of expansion we enhance the background pressure. The stronger the expansion, the larger the background pressure.

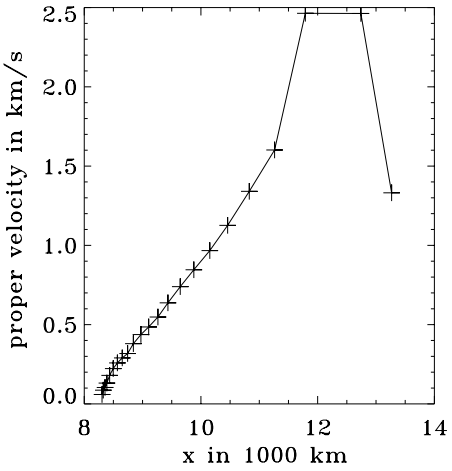

Fig. 7. Proper motion of the footpoint. The apparent inward velocity of the migrating footpoint is plotted versus the radial distance x from sunspot center. The plus signs are equally spaced in time ($\triangle t = 300$s), tracing the evolution between $t = 300$ s ($x = 13\,300$ km) and $t = 7\,200$ s ($x = 8\,300$ km).

3.2.6. Final stages of the simulated evolution

As discussed in Sect. 3.2.3, plasma within the tube expands as it rises through the convection zone. Thereby, the magnetic field strength, B, decreases. The magnetic field strength of plasma reaching the footpoint is the smaller, the larger is the height difference it traveled through the convection zone. That implies, that $v_{\rm A} = B/\sqrt{4\pi\rho}$ at the footpoint decreases continuously, while the flow velocity stays constant in time at the footpoint. Hence, at some point (in our simulation at $t \approx 7\,000$ s) the flow becomes superalfvénic and the centrifugal force exceeds the magnetic tension force at the turning point, i.e. the flow overshoots the turning point. Due to radiative losses in the atmosphere, the plasma that overshoots gets denser and decelerates.

The amplitude of the overshoot gradually increases in time as $v_\parallel/v_{\rm A}$ increases. Once the flux tube dives back into the convectively unstable subphotospheric penumbra, anti-buoyancy drags the tube down, and magnetic tension is too weak to prevent the tube from sinking. Fig. 6b shows a snapshot of the tube in the vicinity of the turning point after 9 300 s. The inertia of the upflow at the footpoint prevents the turning point from sinking. The part of the tube that dives back beneath the photosphere sinks down. Since the radii of curvature at the turning point ($x \approx 8.4$ Mm) and at $x \approx 10.2$ Mm become very small, the thin flux tube approximation is no longer valid. For that reason, we stop the simulation here.

4. Observational consequences

In order to discuss the observational consequences of our model, we concentrate on the evolution of the tube in and above the photosphere, since only here is the tube observable. Fig. 7 shows the proper inward velocity of the migrating footpoint as a function of the radial distance x from sunspot center. It illustrates the migration of the tube's footpoint which will be compared with the observed inward migration of bright penumbral grains. Further, we use Fig. 8 to discuss the features of our simulations in the context of the observed penumbral fine structure such as bright and dark filaments and the Evershed effect. It shows an intermediate stage of evolution of the tube near the surface layers. From left to right, one can see the umbra, the penumbra, and the quiet sun being separated by the peripatopause and the magnetopause, respectively. In Fig. 8a, 8c, and 8d the gray coding represents the temperature variation, the gas pressure variation, and the variation of the magnetic field strength, respectively. Note, that in each background stratification the temperature and the pressure vary only with depth, whereas the magnetic field is two-dimensional. Fig. 8b shows the optical thickness of the tube. Here, the subphotospheric background is illustrated as an optically thick regime and the atmosphere as an optically thin regime. For better visibility the diameter of the tube in Fig. 8 has been magnified by a factor 6. The arrows inside the tube indicate longitudinal flow velocities. Just below the footpoint a velocity of 3 km s^{-1} is present, beyond the footpoint the velocity increases to 6 km s^{-1}, and at the outer part of the penumbra near $x = 12$ Mm the flow velocity reaches 13 km s^{-1}.

4.1. Penumbral grains and bright filaments

The footpoint of the flux tube can be identified with a bright penumbral grain, because the upflow along the tube brings hot plasma to the surface which appears bright against the darker background. As demonstrated in the previous section, the tube's footpoint migrates from the outer edge of the penumbra inward towards the umbra. In Fig. 7 the data points (plus signs) are equally spaced in time ($\triangle t = 300$ s), illustrating that the footpoint starts off at $x = 13\,300$ km with a proper velocity exceeding 2 km s^{-1}. After 1 200 s (4$^{\rm th}$ data point from the right) the migration of the footpoint decelerates from 1.5 km s^{-1} to ≈ 0.1 km s^{-1} at $t = 7\,200$ s. These values are consistent with the proper motion of penumbral grains observed by Muller (1973b).

At the footpoint, the tube's temperature and gas pressure are higher than the corresponding background values. As the plasma flows along, the tube loses internal energy by radiation. Thereby it cools and the gas pressure diminishes. At $x \approx 10$ Mm it reaches temperature equilibrium with the surroundings. As the gas pressure diminishes, the magnetic field strength increases according to Eq. (13), and flux conservation, Eq. (11), implies that the tube's diameter decreases between the footpoint and the point of thermal equilibrium. Thus, our model is concurrent with observations from Muller (1973a, b) and Tritschler et al. (1997) which show that penumbral grains consist of a bright coma and a somewhat dimmer thinner tail which is radially elongated and points away from the umbra. Our model suggests that bright filaments are the long tails of penumbral grains. However, for lower spatial resolution, a few radially aligned penumbral grains might also be visible and interpreted as one bright filament. We want to mention, that the length of the bright tail depends on the amount of magnetic flux of the tube: More magnetic flux implies a larger diameter and thus a larger optical depth,

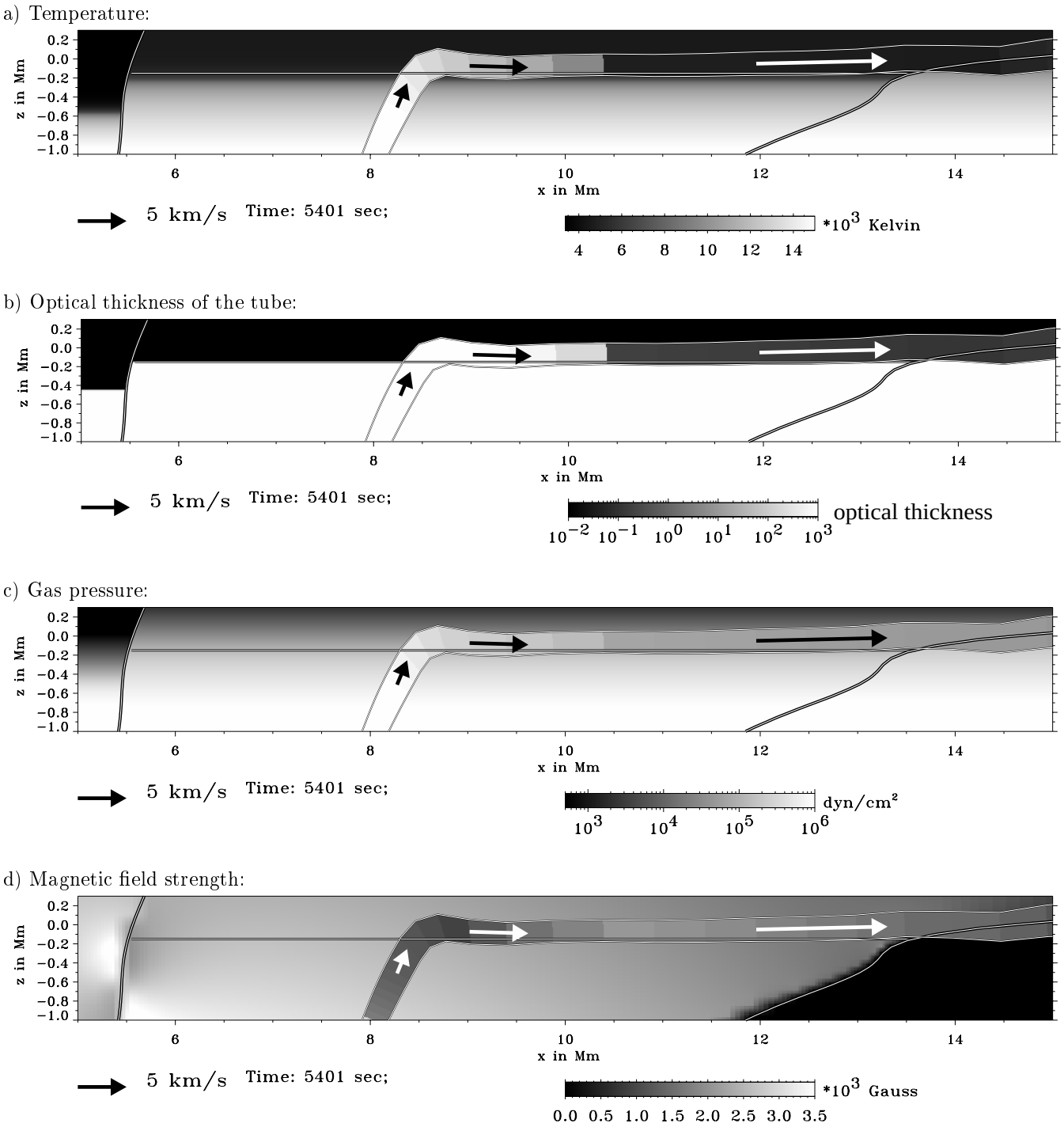

Fig. 8a–d. Snapshot of the evolution at $t = 5\,400$ s. From left to right one sees the umbra, the penumbra, and the quiet sun. The tube that has risen from the magnetopause lies horizontally above the photosphere, being elevated some 100 km. The tube's diameter is magnified by a factor 6 for better visibility. As indicated by the legends, the gray coding represents physical variables along the tube and in the background: **a** Temperature, **b** Optical thickness of the tube, **c** Gas pressure, **d** Magnetic field strength. The arrows in the tube visualize longitudinal velocities in the tube. In the lower left corner of each plot an arrow with a length that corresponds to 5 km s^{-1} is shown.

a longer radiative relaxation time (see Eq. (25)), and hence a longer bright tail.

4.2. Dark filaments

In view of Figs. 8a and 8b, one can see that the tube is optically thick as long as it is hotter than the surroundings. This is due to the temperature dependence of the H^- opacity which

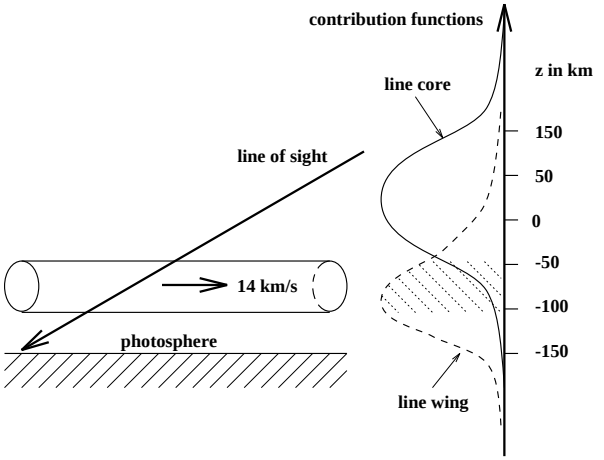

Fig. 9. Explanation of line asymmetries. A thin flow channel only affects parts of a typical photospheric absorption line. As it is drawn in this figure, the flow channel Doppler-shifts a fraction of the contribution function for the line wing, but does not influence the contribution function of the line core, leaving the line core unshifted. Hence, a thin flow channel can naturally explain the observed line asymmetry which is a characteristic feature of the Evershed effect.

is the dominant opacity near the photosphere: $\tilde{\kappa} \propto T^9$. Another important feature was already mentioned in Sect. 3.2.2: The tube is elevated above the photosphere. That means that bright filaments are optically thick structures overlying a darker background and surrounded by an optically thin atmosphere. Therefore, we propose that dark filaments might not exist *per se*. They rather appear as a consequence of spacing between radially elongated bright filaments (Schlichenmaier et al. 1998). This is consistent with the statement of Muller (1973a, 1973b) that within the penumbra bright features *show up* against a dark background.

4.3. Evershed effect

Our model also offers a consistent explanation for the Evershed effect: Between the footpoint, at $x \approx 10.5$ Mm, and the outer edge of the penumbra, the matter inside the tube becomes gradually more transparent. The optical thickness of the tube decreases to $\tau \approx 10^{-1}$ (see Fig. 8b) and a line of sight that crosses the tube reaches optical depth $\tau = 2/3$ in the photosphere of the model at $z = -150$ km, i.e. below the tube. In other words, after the plasma has cooled reaching temperature equilibrium with the surroundings, the tube becomes transparent. The tube constitutes a flow channel that is elevated approximately 100 km above the photosphere and confines an outward flow reaching velocities up to 13 km s^{-1}. In the following we discuss the influence of such a flow channel on the line profiles of photospheric absorption lines.

Generally speaking, a flow channel Doppler-shifts a line profile that is formed inside the flow channel. In order to understand the line asymmetry which is a characteristic feature of the Evershed effect, one should recall that the contribution function of the line core has its maximum higher up in the atmosphere than the contribution function of the line wing, as it is depicted for a typical photospheric absorption line in Fig. 9. Since the flow channel might be substantially thinner than the width of the corresponding contribution function, only distinct parts of a line profile might be shifted. Therefore, a line asymmetry would be caused naturally by a thin flow channel. A line asymmetry which is such that the line wing is more shifted than the line core (see Fig. 1b of Degenhardt 1993) can be explained by a flow channel that is sufficiently thin and is elevated only slightly above the photosphere (Schlichenmaier et al. 1998): Such a flow channel affects the contribution function of the line wing, but does not influence the contribution function of the line core which originates in still higher layers.

The diameter of the tube in our simulations is less than 50 km, depending on the strength of the magnetic field. This has to be taken into account, when shifted asymmetric line profiles are interpreted in order to deduce a flow velocity. Wiehr (1995) deduces a flow velocity of ≥ 5 km s^{-1} by assuming that the line asymmetry is caused by a spatially unresolved line satellite being caused by a flow channel. If one further takes into account, that a typical contribution function has a full width at half maximum of more than 100 km and that our simulated tube has a diameter of less than 50 km, a local flow velocity exceeding 10 km s^{-1} may still be consistent with observation.

4.4. Outward flow in bright filaments

In the preceding section we have demonstrated that the outward flow in the transparent cooler part of the tube can reproduce a line profile that is shifted and asymmetric. However, our model also predicts an outward flow in optically thick bright filaments. This result is somewhat surprising, since it is observed that the Evershed flow is correlated with dark filaments (e.g., Beckers & Schröter 1969; Title et al. 1993; Wiehr & Degenhardt 1994) and that bright filaments are anti-correlated with the Evershed flow (Shine et al. 1994). We explain this apparent contradiction by the fact that all these measurements were done using Fe I lines that have a low excitation potential of less than 4 eV. Since these lines originate almost exclusively at atmospheric temperatures of, say, less than 6000 K, we expect that a hot, optically thick flow channel has a negligible contribution to the intensity profile of these lines. If anything, a hot flow channel would at most shift the line wing, where the line intensity is close to the continuum intensity. Hence, a hot flow channel may not be detectable with absorption lines of low excitation potential. On the other hand, absorption lines which are sensitive to high temperatures, i.e. lines which have a higher excitation potential, are expected to originate mainly within a hot flow channel. Hence, observing bright filaments, i.e. hot plasma, it is more appropriate to use a "hot" absorption line with a high excitation potential, such as the C I 538.03 nm line. Since this line has an excitation potential of 7.68 eV, its mere existence within the penumbra indicates that hot plasma is present. In fact, high resolution measurements in the C I 538.03 nm line demonstrate the existence of this line within the penumbra and furthermore, they show line core shifts (Rimmele 1995, Stanchfield et al. 1997). Fig. 5 in Stanchfield

et al. shows line core shifts corresponding to Doppler velocities up to 2 km s^{-1} within the penumbra, being blue-shifted on the center side and red-shifted on the limb side. We take this observation as an indication for the existence of outward flows in bright filaments.

Finally, we want to mention that Wiehr (1995) and Balthasar et al. (1997) find indications for the existence of a non-zero velocity in bright filaments, if line profiles are interpreted in terms of a largely shifted line satellite that stems from dark filaments and a weakly shifted main component that stems from bright filaments.

In order to decide whether a line shift would be produced by the hot part of our model tube, one has to compute synthetic line profiles. Therefore the temperature gradient across the tube is needed, which forms when an optically thick, hot tube radiates in a cooler, optically thin atmosphere. Thus, for computing synthetic line profiles, it is essential to treat the radiative transport for our model tube.

In summary, our model suggests that there are three different structures within a penumbra: a) a bright component, in which the optically thick and hot flow may only be detectable using "hot" absorption lines, b) a dark component, in which a flow channel of small optical thickness lies above the dark background, and c) a dark component consisting of the dark background with no flux tube above it. In the last component one would see a dark filament with no Evershed flow present, whereas in case b) one would look at a dark filament which contains the flow. Hence, the Evershed signal is correlated with some but not all dark filaments.

5. Discussion

We have presented a numerical simulation of the time dependent dynamic evolution of a thin magnetic flux tube inside a sunspot penumbra. The results yield an extension of the studies reported by Jahn et al. (1996), and Schlichenmaier et al. (1997). Here, we aim at a more detailed understanding of the physical structure of the penumbra. Since our model seems to reproduce the observed small-scale structure of the penumbra, we take this as an indication that it supports the concept of interchange convection, on which our results are based. The model suggests:

1. Penumbral grains are the footpoints of inwards migrating flux tubes, in which the enhanced brightness is caused by a systematic upflow. At the footpoint an upflow of 3 km s^{-1} is present.
2. A bright filament, when interpreted as the dimmer and thinner tail of a penumbral grain, is the consequence of a hot plasma outflow that cools down during horizontal outward motion. Bright filaments are hotter and optically thicker than the surroundings, and are elevated relative to the dark background. In bright filaments a plasma flow is present having a velocity of typically 6 km s^{-1}.
3. The dark background is partly eclipsed by bright filaments. Hence, the appearance of dark filaments would be the result of spacing between bright filaments.
4. The Evershed flow occurs with velocities up to 13 km s^{-1} in optically thin ($\tau \approx 10^{-1}$) and almost horizontal channels which are elevated some 100 km above the photosphere.

In our model, the magnetic flux tube and the corresponding plasma flow extends beyond the outer penumbral boundary. At the boundary, the tube follows the magnetopause, which slowly gains height and reaches $z = 700$ km at $x = 27$ Mm. There, the boundary condition allows for a steady outflow of mass. Thus, our model does not describe magnetic flux tubes that dive back beneath the photosphere near the outer edge of the penumbra, as recently reported by Westendorp Plaza et al. (1997) and Stanchfield et al. (1997). Modeling dynamical flux tubes that bend back down near the outer edge of the penumbra requires different upper and lower boundary conditions. Instead, our model describes the part of the Evershed flow which continues up into the canopy, as it was observed by Solanki et al. (1994).

So far, we have only considered the rise of a tube that lies along the magnetopause initially. Clearly, for an understanding of interchange convection, we need not only study different initial conditions, but also the dynamics of sinking magnetic flux tubes. If no sinking tubes were present, magnetic flux would be transported continuously from the outer to the inner part of the penumbra. In consequence, the magnetic pressure would increase in the inner part of the penumbra. We surmise that at some point, the gradient of the magnetic pressure, $\nabla B_{\rm b}^2/8\pi$, becomes large enough to suppress the further rise and to initiate the sinking of the flux tube.

We want to stress that the acceleration process that causes the outward flow is related to the siphon flow mechanism (Meyer & Schmidt 1968), in the sense that a gas pressure gradient accelerates the plasma. However, in our model the pressure gradient is created locally within the penumbra: The flow is initiated by the rise of a magnetic flux tube and is driven by the superadiabatic background stratification. In the horizontal part of the tube, radiative cooling sustains the gas pressure gradient that accelerates the plasma from 3 km s^{-1} near the footpoint up to 14 km s^{-1} near the outer edge of the penumbra. In result, our model does not require strong magnetic fields at the outer footpoint as in the classical siphon flow scenario. We find an acceleration mechanism that is caused naturally in a certain phase of the evolution of an emerging magnetic flux tube.

Since our simulations yield upflows along subphotospheric flux tubes, it is tempting to speculate that the surplus brightness of the penumbra as compared to the umbra is caused by these upflows which constitute a convective heat transport. Thus, one would suppose that penumbral grains and bright filaments which are fed by these upflows cause small fractions of the penumbra to be brighter than the umbra.

Acknowledgements. RS wishes to thank Prof. Haerendel for fruitful discussions and for supporting this work. KJ acknowledges the support of the KBN by the grant No. 2 P03D 010 12.

References

Balthasar H., Schmidt W., Wiehr E., 1997, Sol. Phys. 171, 331

Bumba V., 1960, Izv. Krymk. Astrofiz. Observ. 23, 253
Beckers J.M., Schröter E.H., 1969, Sol. Phys. 10, 384
Caligari P., Moreno Insertis F., Schüssler M., 1995, ApJ 441, 886
Defouw R.J., 1976, ApJ 209, 266
Degenhardt D., 1991, A&A 248, 637
Degenhardt D., 1993, A&A 277, 235
Evershed J., 1909, MNRAS 69, 454
Ferriz Mas A., 1988, Phys. Fluids 31, 2583
Ferriz Mas A., Schüssler M., 1989, Geophys. Astrophys. Fluid Dynamics 48, 217
Grossmann–Doerth U., Schmidt W., 1981, A&A 95, 366
Holmes J., 1963, MNRAS 126, 155
Huebner W.F., Merts A.L., Magee N.H.Jr., et al., 1977, Los Alamos Sci. Lab. Rep. No. LA-6769-M
Jahn K., 1989, A&A 222, 264
Jahn K., 1992, in: Sunspots, Theory and Observations, eds. J.H. Thomas, N.O. Weiss, Dortrecht, Kluwer, p. 139
Jahn K., Schmidt H.U., 1994, A&A 290, 295
Jahn K., Schlichenmaier R., Schmidt H.U., 1996, Astro. Lett. and Communication 34, 59
Lites B.W., Elmore D.F., Seagraves P., et al., 1993, ApJ 418, 928
Meyer F., Schmidt H.U., 1968, Z. f. angew. Math. Mech., 48, 218
Moreno Insertis F., 1986, A&A 166, 291
Muller R., 1973a, Sol. Phys. 29, 55
Muller R., 1973b, Sol. Phys. 32, 409
Muller R., 1992, in: Sunspots, Theory and Observations, eds. J.H. Thomas, N.O. Weiss, Dortrecht, Kluwer, p. 175
Priest E.R., 1982, Solar Magnetohydrodynamics, D. Reidel Publishing Company, Dortrecht
Rimmele T.R., 1995, A&A 298, 260
Rucklidge A.M., Schmidt H.U., Weiss N.O., 1995, MNRAS 273, 491
Schlichenmaier R., 1997, Dissertation, Ludwig-Maximilians-Univ. München, Utz-Verlag, München
Schlichenmaier R., Jahn K., Schmidt H.U., 1997, in: Advances in the physics of sunspots, eds. B. Schmieder, J.C. del Toro Iniesta, M. Vásquez, A.S.P. Conf. Ser. Vol. 118, p. 140
Schlichenmaier R., Jahn K., Schmidt H.U., 1998, ApJ Letters 493, L121
Schmidt H.U., 1987, in: The role of fine-scale magnetic fields on the structure of the solar atmosphere, eds. E.H. Schröter, M. Vásquez, A.A. Wyller, Cambridge University Press, Cambridge, p. 219
Schmidt H.U., 1991, Geophys. Astrophys. Fluid Dyn. 62, 249
Schmidt W., Hofmann A., Balthasar H., et al., 1992, A&A 264, L27
Schröter E.H., 1965, Z. f. Astrophysik 62, 228
Shine R.A., Title A.M., Tarbell T.D., et al., 1994, ApJ 430, 413
Solanki S.K., Montavon C.A.P., Livingston W., 1994, A&A 283, 221
Soltau D., 1982, A&A 107, 211
Spiegel E.A., 1957, ApJ 126, 202
Spruit H.C., 1981a, A&A 98, 155
Spruit H.C., 1981b, A&A 102, 129
Stachnik R.V., Nisenson P., Noyes R.W., 1983, ApJ 271, L37
Stanchfield II D.C.H., Thomas J.H., Lites B.W., 1997, ApJ 477, 485
Stellmacher G., Wiehr E., 1980, A&A 82, 157
Stix M., 1989, The Sun, Springer Verlag, Berlin
Thomas J.H., 1988, ApJ 333, 407
Thomas J.H., Montesinos B., 1993, ApJ 407, 398
Title A.M., Frank Z.A., Shine R.A., et al., 1993, ApJ 403, 780
Tritschler A., Schmidt W., Knölker M., 1997, in: Advances in the physics of sunspots, eds. B. Schmieder, J.C. del Toro Iniesta, M. Vásquez, A.S.P. Conf. Ser. Vol. 118, p. 170
Westendorp Plaza C., del Toro Iniesta J.C., Ruiz Cobo B., et al., 1997, Nat 389, 47
Wiehr E., 1995, A&A 298, L17
Wiehr E., Degenhardt D., 1994, A&A 287, 625